



## Surface-modified GVs as nanosized contrast agents for molecular ultrasound imaging of tumor



Guohao Wang<sup>a,1</sup>, Lin Song<sup>a,1</sup>, Xuandi Hou<sup>a</sup>, Shashwati Kala<sup>a</sup>, Kin Fung Wong<sup>a</sup>, Liya Tang<sup>a</sup>, Yunlu Dai<sup>b</sup>, Lei Sun<sup>a,\*</sup>

<sup>a</sup> Department of Biomedical Engineering, The Hong Kong Polytechnic University, Hung Hom, Hong Kong Special Administrative Region

<sup>b</sup> Cancer Centre, Faculty of Health Sciences, University of Macau, Macau

### ARTICLE INFO

#### Keywords:

Gas vesicles  
Ultrasound  
Tumor diagnosis  
Contrast agents  
Molecular imaging

### ABSTRACT

Nanobubbles, as a kind of new ultrasound contrast agent (UCAs), have shown promise to penetrate tumor vasculature to allow for targeted imaging. However, their inherent physical instability is an ongoing concern that could weaken their imaging ability with ultrasound. Gas vesicles (GVs), which are genetically encoded, naturally stable nanostructures, have been developed as the first ultrasonic biomolecular reporters which showed strong contrast enhancement. However, further development of tumor imaging with GVs is limited by the quick clearance of GVs by the reticuloendothelial system (RES). Here, we developed PEGylated HA-GVs (PH-GVs) for in-tumor molecular ultrasound imaging by integrating polyethylene glycol (PEG) and hyaluronic acid (HA) in GV shells. PH-GVs were observed to accumulate around CD44-positive cells (SCC7) but not be internalized by macrophage cell line RAW 264.7. Green fluorescence from PH-GVs was found around cell nuclei in the tumor site after 6 h and the signal was sustained over 48 h following tail injection, demonstrating PH-GVs' ability to escape the clearance from the RES and to penetrate tumor vasculature through enhanced permeability and retention (EPR) effects. Further, PH-GVs produced strong ultrasound contrast in the tumor site *in vivo*, with no obvious side-effects detected following intravenous injection. Thus, we demonstrate the potential of PH-GVs as novel, nanosized and targeted UCAs for efficient and specific molecular tumor imaging, paving the way for the application of GVs in precise and personalized medicine.

### 1. Introduction

The emergence of molecular imaging for cancer diagnosis and monitoring is considered a major milestone in the field of medical imaging [1]. Molecular imaging allows the noninvasive and continuous monitoring of tumors at the cellular and molecular levels [2–4]. Ultrasound imaging, the most commonly-used non-invasive imaging modality in clinics, has the advantages of low cost, wide availability, outstanding safety profile, lack of ionizing radiation, high spatio-temporal resolution, and portability [5–7]. The development of targeted ultrasound contrast agents (UCAs) enables ultrasonic molecular imaging and extends the diagnostic capability and utility of this traditional imaging mode [8]. Commercial UCAs are usually gas-filled microbubbles, surface-modified with ligands that can target cells specifically, thereby significantly increasing the sensitivity and specificity of ultrasound imaging [9]. Since microbubbles are several micrometers

(1–8  $\mu\text{m}$ ) in diameter, they remain exclusively within the vascular compartment and this property makes them particularly well-suited for intravascular imaging of inflammation, angiogenesis, thrombi etc. [10]. Although the utilization of microbubbles for ultrasound imaging has shown encouraging results, their potential utility in biomedicine has been constrained by their inability to pass through vessel walls into non-vascular tumor sites [1,8,11].

Nanobubbles, due to their nanoscale size, have greater potential in extravascular molecular applications such as tumor imaging. It is well-established that tumor vasculature exhibits enhanced permeability and retention (EPR) effects and nano-sized particles could efficiently cross the leaky, defective vasculature of tumors, leading to high extravasation and retention of nanoparticles in the tumor site [12]. Recently, targeted and non-targeted nanobubbles with various shells such as phospholipids or polymers have been developed for molecular ultrasonic imaging of tumors [13,14]. Despite their potential benefits in

\* Corresponding author. Room ST409, Department of Biomedical Engineering, Faculty of Engineering, The Hong Kong Polytechnic University, Hong Kong Special Administrative Region.

E-mail address: [lei.sun@polyu.edu.hk](mailto:lei.sun@polyu.edu.hk) (L. Sun).

<sup>1</sup> These authors contributed equally to this work.

tumor-targeted imaging, their configuration needs stabilization by the addition of surfactant on the shells as well as by the perfluorocarbon gas core [15–18]. Gas escape, bubble fragmentation, and nanobubble collapse are phenomena that could occur after *in vivo* administration, negatively affecting their imaging performance.

Gas vesicles (GVs) are nanoscale gas-filled protein structures expressed intracellularly in certain cyanobacteria, which were recently reported as gene-encoded reporters offering significant potential as molecular ultrasound contrast agents [19–22]. Unlike traditional UCAs, which trap preloaded gas in an unstable configuration, the 2 nm-thick protein shells of GVs exclude water but are freely permeable to gases in the surrounding media, making them physically stable despite their nanometer size [19,23]. GVs were demonstrated to be able to produce robust ultrasound contrast across a range of frequencies at picomolar concentrations and exhibit harmonic scattering to enable enhanced detection versus background *in vitro* [19,22]. Moreover, strong non-linear contrast images of GVs could be acquired on the location of inferior vena cava (IVC) and liver after intravenous injection [19]. Their stable performance and robust ultrasound contrast make GVs good candidates as molecular contrast agents for tumor imaging. However, similar to other common nanoparticles, the majority of GVs after intravenous administration is usually taken up in non-targeted tissues, such as the liver, spleen, and lungs [24]. Foster et al. recently reported that the reticuloendothelial system (RES) cleared 84% of native GVs 20 min following administration to mice due to capture by phagocytic cells and collapsed GVs through the biliary system, with almost no GVs remaining in the blood 120 min after injection [24]. Such rapid clearance could limit the utility of GVs for tumor molecular imaging as they may not be able to circulate long enough to extravasate into tumor tissues.

Surface modifications can be made to GVs to resolve the systemic clearance issue by improving their pharmacokinetic properties. Multiple studies have reported that adding polyethylene glycol (PEG) on the surface of nanoparticles effectively reduced RES uptake and increased circulation time in the blood, leading to selective accumulation of the nanoparticles to the tumor site [25–28]. Likewise, hyaluronic acid (HA) on the surface of nanoparticles has displayed efficacy in targeting particles to CD44-positive malignant cancer cells and selectively enhancing the accumulation and retention of nanoparticles at the tumor site [29–33]. In the present study, PEG-conjugated-HA was conjugated to GVs and the PEGylated HA-GVs (PH-GVs) were characterized. PH-GVs abd GVs were found to be stable in solution as well as when under ultrasound irradiation. PH-GVs were found to display enhanced targeting and immune escape abilities compared to unmodified GVs, and were not cytotoxic to cells. PH-GVs also showed greater tumor targeting and retention as well as longer duration of sustained signal *in vivo*, without obvious damage to vital organs. Thus, in all, we demonstrate PH-GVs as a potent novel nanoparticle for ultrasound molecular imaging *in vivo* with high biocompatibility and targeting ability.

## 2. Results and discussion

### 2.1. Characterization of native GVs and PEGylated HA-GVs (PH-GVs)

The PH-GVs used in this study were generated by sequential covalent conjugation of HA followed by PEG to native GVs harvested from *Anabaena flos-aquae* (Fig. 1). The successful synthesis of PH-GVs was confirmed by transmission electron microscopy (TEM). Compared to native GVs which showed clean cylindrical morphology and clear ribs on the shell, PH-GVs were wrapped by a layer of substrate and the ribs on the shell were not easily visible (Fig. 2a). Zeta potential of native GVs was between  $-40 \pm 5$  mV while PH-GVs showed an negative zeta potential of  $-20 \pm 6$  mV (Fig. 2b). Zeta potential is a key indicator of nanoparticle stability, and the values obtained for both native GVs and PH-GVs indicated a suitable surface charge for colloidal stability [34]. Both GV groups showed nanoscale diameters ( $\sim 400$  nm for native GVs,

$\sim 500$  nm for PH-GVs) with relatively uniform size distributions (Fig. 2c).

### 2.2. Ultrasound imaging properties of PH-GVs

GVs and PH-GVs were next tested for their ultrasound contrast properties using a Vevo 2100 imaging system (FUJIFILM VisualSonics, B-mode) operating at 21 MHz, at different concentrations. Both native GVs and PH-GVs produced robust contrast relative to buffer controls at concentrations ranging from 250 to 1000 pM, with gas volume fractions of approximately 0.01%–0.1% (Fig. 3a). Contrast in both GVs groups increased as the concentration of GVs was increased, with 1000 pM showing the highest contrast in both groups (Fig. 3b). We also determined the biostability of the GV groups by incubating them in PBS or fetal bovine serum (FBS) and imaging them over the course of 7 days. Native and PH-GVs showed no reduction in echogenicity in either PBS or FBS, thereby demonstrating their physical stability in physiologically relevant conditions (Fig. 3c and d). These results demonstrate that native and PH-GVs generated by us showed good contrast generation and stability in solution. Besides, we tested the stability of PH-GVs under some physical or mechanical forces, such as temperature, ultrasonic. We conducted additional experiment to demonstrate the stability of GVs and PH-GVs under different conditions (25 °C, 37 °C, 45 °C) for different time durations, and examined the ultrasound contrast intensity. The echoed ultrasound signals were captured in B-mode images (Fig. S1a) and quantitative intensity chart (Fig. S1b) shown below. The results show that the ultrasound intensity of GVs and PH-GVs remained stable for up to 24 h at all temperatures without obvious decreasing trend. In another experiment, B-mode images were acquired under ultrasound irradiation at imaging intensity level at different time points. The results in Figs. S1c and S1d show no echo contrast decrease of both GVs and PH-GVs, indicating GVs and PH-GVs are stable enough under B-mode imaging intensity. GVs used in the study is *Ana* GVs, and the critical collapse pressure is 440–605 kPa [19]. When applying 650 kPa ultrasound sonication, both GVs and PH-GVs collapsed with immediate echo signal disappeared (Fig. S1c). Both GVs and PH-GVs collapsed with 650 kPa insonation.

### 2.3. Targeting ability and immune escape ability of PH-GVs *in vitro*

To validate the active targeting efficiency of PH-GVs, we incubated our PH-GVs with the squamous cell carcinoma cell line (SCC7), known to have high expression of CD44. To monitor the location of our GVs, we labeled both groups of GVs with indocyanine green (ICG), a near infra-red (NIR) fluorophore (Fig. S2a). ICG-linked GVs showed a significant broadening of their absorption spectrum compared to free ICG, indicating their successful conjugation (Fig. S2b). ICG-linked GVs also showed significantly higher fluorescence intensity at increasing concentrations, thereby confirming the successful linkage of the dye to the GVs (Figs. S2c–d). The interaction of ICG labeled native GVs and PH-GVs with CD44-positive cells was then evaluated using fluorescence imaging. ICG-PH-GVs showed a significantly greater ability to accumulate in the cytoplasm of SCC7 cells than the ICG-GVs after 6 h incubation (Fig. 4a) indicating more successful cellular uptake of the PH-GVs. We also tested the GV groups' immune escape abilities *in vitro* by incubating them with the murine macrophage cell line RAW 264.7. Native GVs showed a strong red fluorescence within these immune cells, while PH-GVs showed little-to-no signal (Fig. 4b) indicating enhanced immune escape of the PH-GVs. PEGylation of HA-GVs was thus seen to confer greater homotypic targeting and reduced internalization by immune cells with greater potential for effectiveness *in vivo*.

### 2.4. Biodistribution and tumor accumulation of PH-GVs *in vivo*

Next, we determined the *in vivo* biodistribution and tumor-targeting characteristics of PH-GVs. Tumor-bearing mice were monitored for 48 h

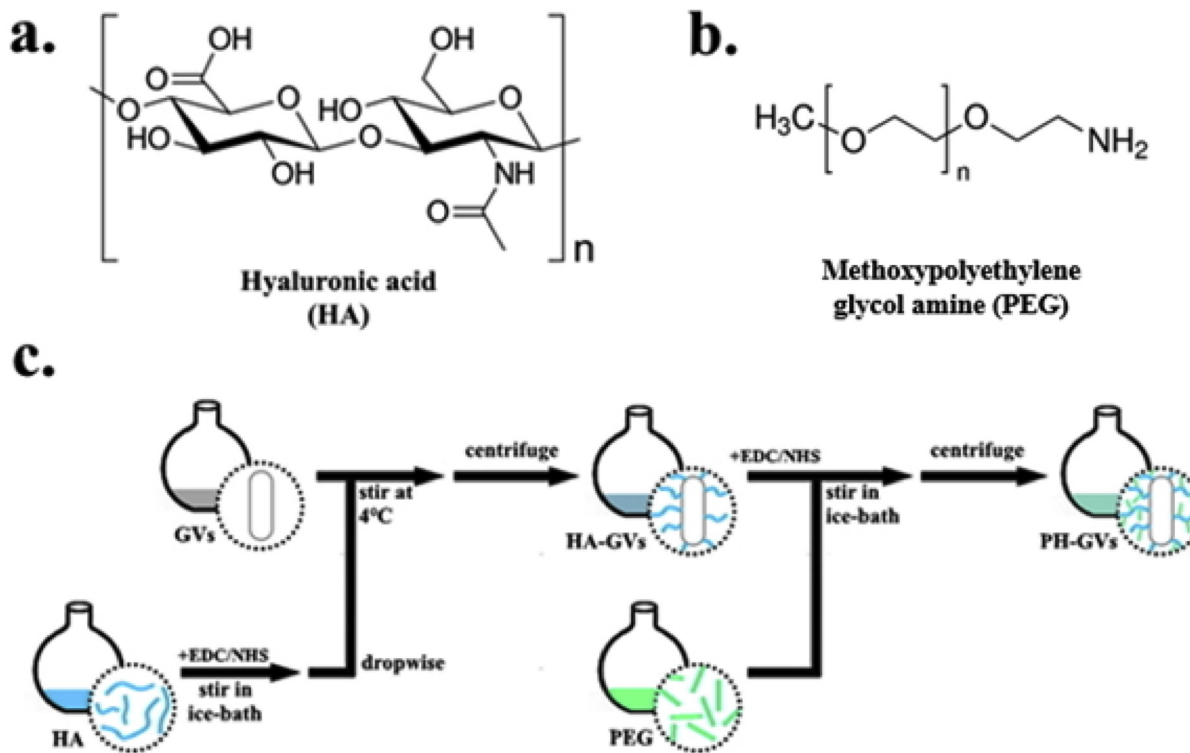


Fig. 1. Schematic illustration of the preparation process of PEGylated HA-GVs (PH-GVs).

by real-time NIRF imaging after systemic administration of free ICG (200  $\mu$ L, 20  $\mu$ g), ICG-labeled GVs (20 nM, containing 20  $\mu$ g ICG), ICG-labeled HA-GVs (20 nM, containing 20  $\mu$ g ICG) and ICG-labeled PH-GVs (20 nM, containing 20  $\mu$ g ICG) respectively. Free ICG and ICG-labeled GVs initially showed significant fluorescence in the vital organs (liver, lungs, spleen, etc.), but decreased over time without showing localization in the tumor site (Fig. 5a). In ICG-labeled HA-GVs group, strong signals around the whole body of the mice were detected at the early time points. By contrast, ICG-labeled PH-GVs showed consistent but moderate signals in the vital organs of mice at the shortly post-injection but showed the strongest localization to the tumor site from 8 h onwards. 6 h post-administration, ICG-labeled PH-GVs showed a Tumor/Muscle ratio above 2 and was maintained for almost all of the remaining duration, which is always higher than that of ICG-labeled HA-GVs group (Fig. 5b). This ratio did not significantly increase in Free ICG and GVs groups at any point. Closer examination of the large organs and the tumor showed that ICG-labeled PH-GVs group showed high fluorescence in the tumor at 12, 24 and 48 h but not in the other vital organs, whereas ICG-labeled GVs localized highly in the liver, but not in the tumor at any observed time point (Fig. 5c). The fluorescence intensity of tumor in ICG-labeled PH-GVs group remained high over the 48 h period examined, whereas fluorescence of tumor decreased in ICG-labeled GVs group and ICG-labeled HA-GVs group over time indicating tumor excretion gradually (Fig. 5d-f). The ability of PH-GVs to primarily label the tumor site after 6 h and the sustained signal over 48 h confirmed the PH-modification's improvement to the ability of the PH-GVs to escape immune clearance, their stability, and their tumor-targeting potential.

To further confirm the enhanced retention of ICG-labeled PH-GVs in tumor-bearing mice, we finally investigated the interstitial penetration of ICG-labeled GVs and ICG-labeled PH-GVs inside solid tumors after 12 h post-injection. The tumors were extracted and tumor slices were stained with DAPI (blue) and anti-CD31 antibody (red) for confocal imaging to label the relative location of cell nuclei and blood vessels. ICG-labeled GVs showed no fluorescence (green) in the tumor sections, whereas strong ICG fluorescence was visible in the tumors of the ICG-

labeled PH-GV group (Fig. 5g). Crucially, the green fluorescence observed was not restricted to colocalization with CD31 (vessels) but could also be seen in the region around the nuclei. This indicates the successful passing of the PH-GVs past the tumor vasculature, through the EPR effect, and successful cellular uptake by tumor cells. Combined with the evidence detailed in previous figures, these results demonstrate that the PH-encapsulation of GV surfaces enabled reduced clearance, enhanced blood circulation time and increased tumor penetration through blood vessels, enabling their enhanced *in vivo* performance.

## 2.5. *In vivo* cancer US imaging by PH-GVs

We next tested the GVs groups' relative abilities to generate US contrast *in vivo* by intravenously injecting GVs, HA-GVs or PH-GVs into SCC7 tumor-bearing mice. 200  $\mu$ L GV, HA-GVs and PH-GVs (20 nM) were respectively administered into the tail vein of tumor-bearing nude mice and nonlinear ultrasound images (transmitting at 18 MHz) of the tumor site were acquired using the Vevo 2100 imaging system. Ultrasound images showing tumor sites at 0, 0.5, 1, 2, 4, 8, 12, 24, and 48 h post-injection showed that PH-GVs showed much greater and well-sustained ultrasound contrast inside the tumor (green signal) compared to native GVs and HA-GVs (Fig. 6a). Imaging with PH-GVs exceeded the ultrasound intensity generated by GVs and HA-GVs at 6 h, peaked at 12 h, gradually diminishing over the remaining period, whereas HA-GVs showed lower ultrasound signals and native GVs showed an almost flat time profile (Fig. 6b). To confirm that PH-GVs were the source of the observed contrast, we applied 650 kPa US pulses, which resulted in the disappearance of the contrast (Fig. 6c). Regions of interest containing GVs exhibited  $60 \pm 14\%$  stronger backscattered signals than buffer-injected controls ( $p = 0.008$ ), with the difference disappearing after collapse ( $p = 0.23$ ) (Fig. 6d).

## 2.6. *In vitro* and *in vivo* toxicity detection

The *in vitro* cytotoxicity of native GVs and PH-GVs on SCC7 cells was

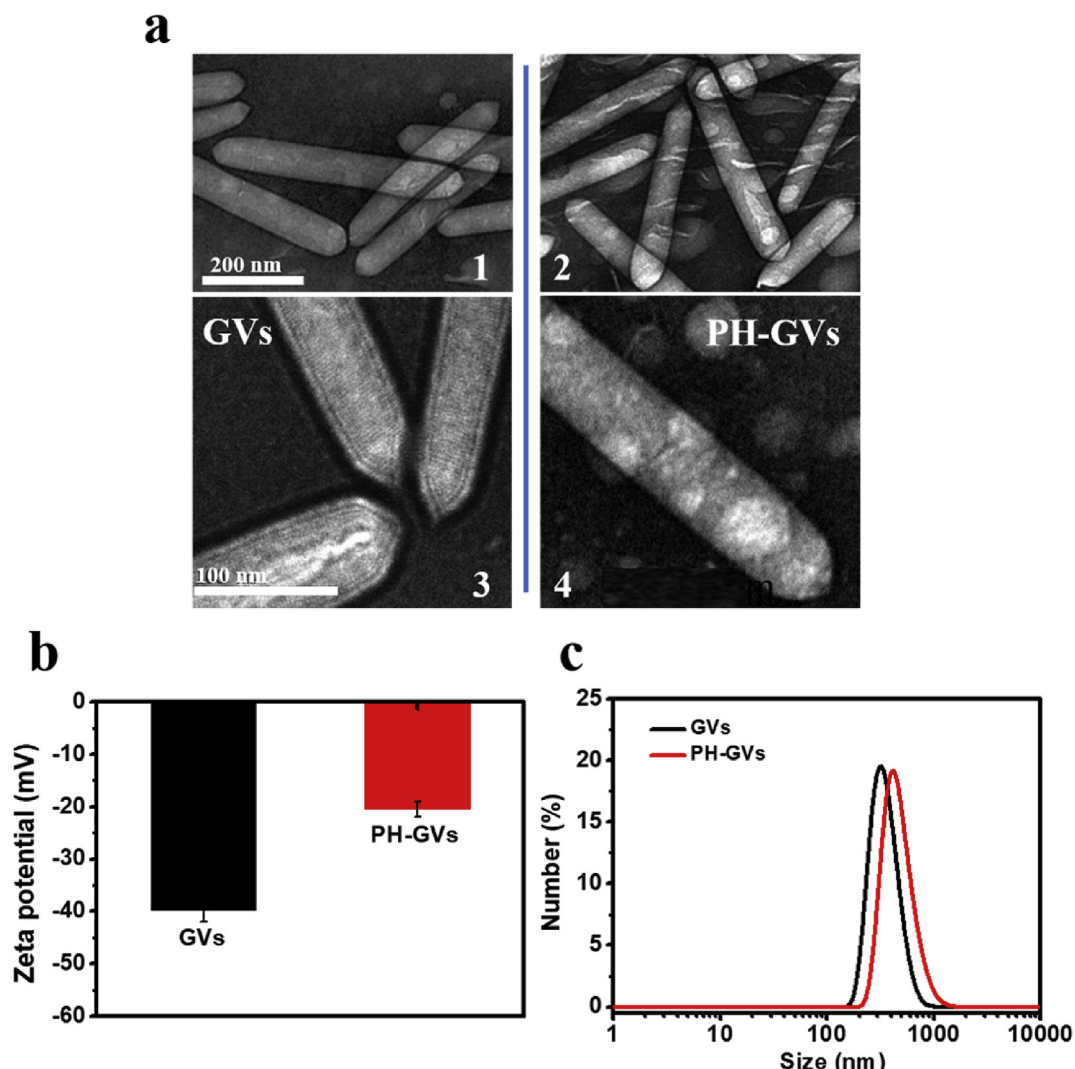


**Fig. 2.** Characterization of GVs and PH-GVs. (a) TEM image of GVs (1, 3) and PH-GVs (2, 4). Scale bar represents 200 nm (1, 2) and 100 nm (3, 4). (b) Zeta potentials of GVs and PH-GVs in PBS. (c) Number-averaged diameter of GVs and PH-GVs in PBS by DLS. Data in (b) and (c) represent the mean  $\pm$  SD from 3 independent experiments.

investigated by incubating them with diverse concentrations of GVs (0–1 nM) followed by a CCK-8 assay. Incubation with native GVs, broken native GVs (collapsed using US) or PH-GVs for 24 h did not induce any noticeable reduction in cell viability at any concentration (Fig. 7a). Incubation with any GV group with incubation time doubled to 48 h also did not result in decreased cell viability at any concentration (Fig. 7b). We thus see that no GV group, including our surface-modified ones, showed any significant cytotoxicity to cells, indicating their general level of safety. We then evaluated the *in vivo* toxicity of the GV treatment on the normal, non-tumor organs of the treated mice by H&E staining. The gross morphology of all vital organs observed in either GV group showed no major differences compared to the PBS control (Fig. 7c). No obvious signs of damage or toxicity were visible in the pathologies of the heart, liver, spleen, lung, and kidneys. The body weights of tumor-bearing mice over the 30-day period of testing were also tracked, and we found that groups of mice injected with GVs or PH-GVs showed no major difference in body weights (Fig. 7d), confirming our *in vitro* observations of non-cytotoxicity.

## 2.7. Conclusion

The search for appropriate contrast agent which is small enough to pass through the vasculature to access the intercellular space of tumors

is a critical concern in the field of molecular ultrasound imaging. In the present study, we successfully synthesized PH-GVs by combining GVs with PEG, which reduced RES uptake and increased blood circulation time, as well as a tumor-targeting ligand-HA. We demonstrated that our synthesized PH-GVs showed good biocompatibility and targetability both in *vitro* and in *vivo*. PH-GVs resulted in reduced uptake in the liver, prolonged blood circulation, selective accumulation at the tumor site, as well as improved tumor targeting effects. Crucially, PH-GVs were seen to be good ultrasound contrast agents in CD44-positive tumor imaging. Such improvements could enable GVs to truly fulfill their potential as a high-performance nanoscale molecular reporter for ultrasound imaging as well as a potential carrier for CD44-positive tumor therapy.

## 3. Materials and methods

### 3.1. Materials

Ethylenediamine (EDA), 1-ethyl-3-(3-(dimethylamino)propyl) carbodiimide (EDC), and Nhydroxysuccinimide (NHS) were obtained from J&K company (Beijing, China). Propidium iodide (PI) was purchased from Sigma-Aldrich Co. (St. Louis, MO). ICG-Sulfo-Osu (ICG) was obtained from Dojindo molecular technologies (Tokyo, Japan). CCK-8

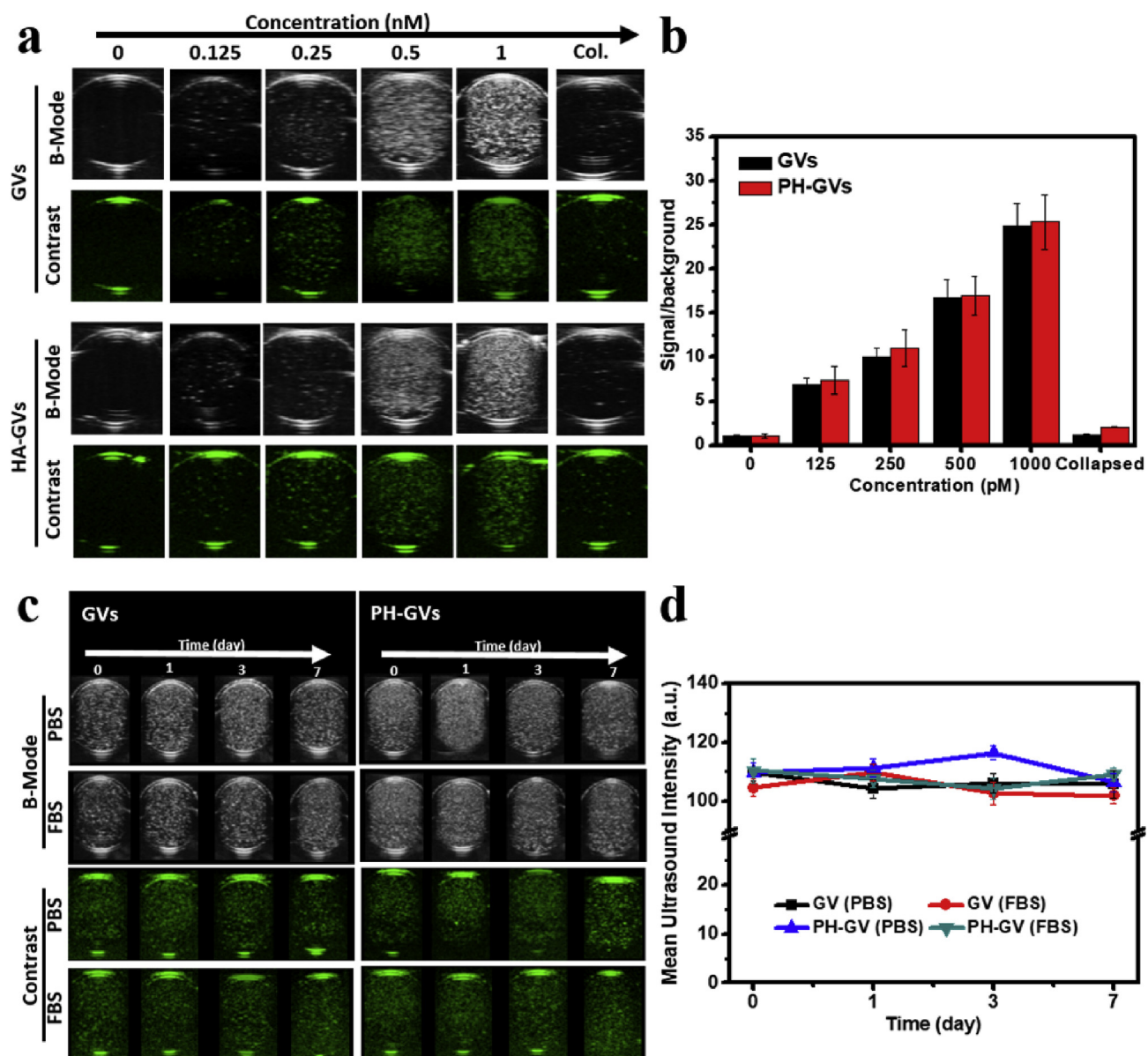


**Fig. 3.** *In vitro* ultrasound image enhancement. (a) Ultrasound images of a dropper phantom containing PBS buffer, GVs, and PH-GVs at concentration ranging from 125 to 1000 pM. Images were acquired at B-mode and contrast mode, as indicated. (b) Total backscattered signal relative to PBS at each GVs concentration. Data represent the mean  $\pm$  SD based on 4 independent experiments. (c) Ultrasound images of a dropper phantom containing GVs and PH-GVs (GVs concentrations of 500 pM) staying for various time. (d) Quantitative analysis of the images in (c). Data represent the mean  $\pm$  SD from 4 independent experiments.

assay kit and 4,6-diamidino-2-phenylindole (DAPI) were purchased from Sangon Biotech (Shanghai, China). Calcein-AM was obtained by Invitrogen (Grand Island NY). FITC-conjugated goat anti-rabbit immunoglobulin G was from Life Technologies (NY, USA). Squamous cell carcinoma cell line (SCC7) were bought from ATCC (Manassas, VA). Methoxypolyethylene glycol amine (PEG-amine, molecular weight = 5 kDa) was purchased from Shanghai Seebio Biotech (Shanghai, China). Sodium hyaluronic acid (HA, molecular weight = 234 kDa) was bought from Lifecore Biomedical (Chaska, MN).

### 3.2. Preparation of native GVs and PEGylated HA-GVs (PH-GVs)

*Anabaena flos-aquae* (FACHB-1255, Freshwater Algae Culture Collection, Wuhan, China) was cultured in sterile BG-11 medium at 25 °C under fluorescent lighting on a 14 h/10 h light/dark cycle. GVs were isolated and purified through tonic cell lysis and centrifugally

assisted floatation according to Walsby's method (Buckland and Walsby 1971). Briefly, hypertonic lysis, achieved by quickly adding sucrose solution to a final concentration of 25%, was used to release GVs. GVs were isolated by centrifugation at 400g for 3 h after hypertonic lysis. The isolated GVs formed a white creamy layer on top of the solution and were collected by syringe. To purify the GVs, it was washed by the same centrifugation process three times and stored in phosphate-buffered saline (PBS) at 4 °C. The concentration of GVs was estimated using a literature-based formula (450 nM per OD500) (Walsby 1994), where OD500 is the optical density at a 500-nm wavelength measured with a UV-visible spectrophotometer (2100 Pro, GE Healthcare, Piscataway, NJ, USA). Volume fraction was estimated using approximated gas volumes of 8.4  $\mu$ L/mg and molar weight of 107 MDa as described elsewhere (Walsby and Armstrong 1979).

For PEGylated HA-GVs (PH-GVs) synthesis, PEG and HA were immobilized to the GVs' protein shells by covalent conjugation. Firstly, EDC (3.37 mg) and NHS (2 mg) were added to HA solution (10 mg) in

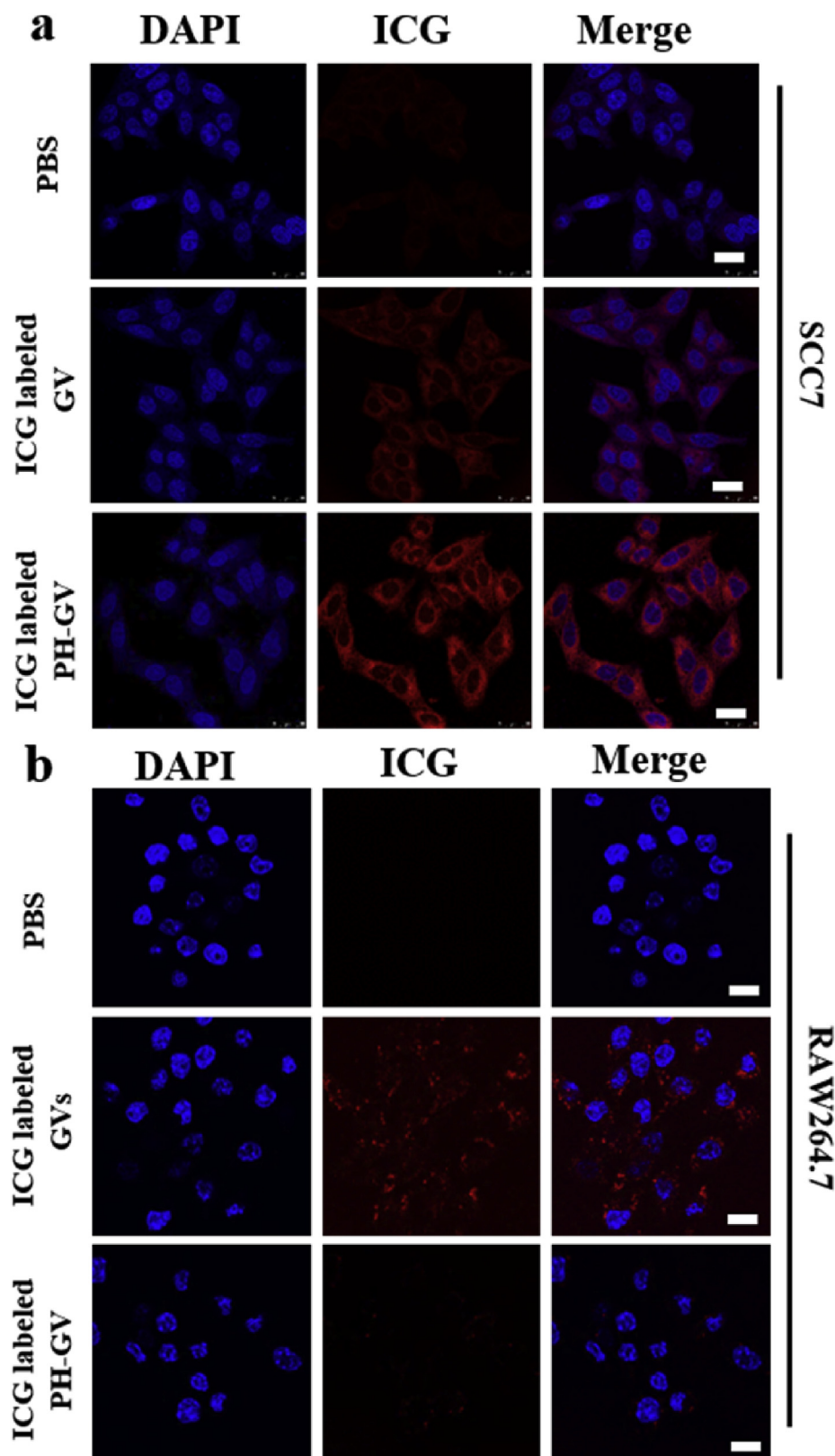
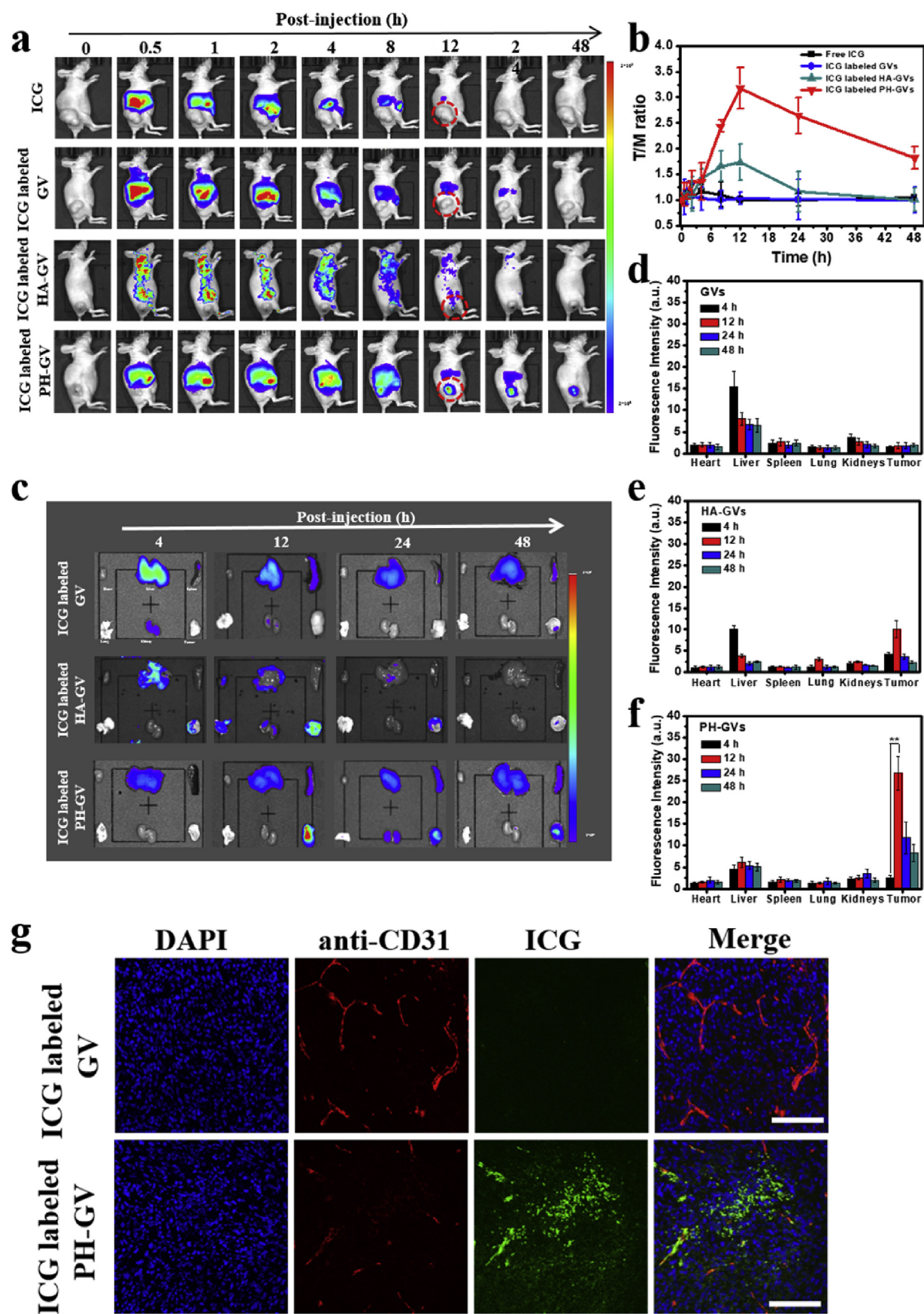


**Fig. 4.** Targeting ability and immune escape abilities of PH-GVs. Confocal microscopy images of ICG labeled GVs and ICG labeled PH-GV co-incubated with SCC7 cells for 6 h. Scale bars represent 20  $\mu$ m. Representative images are shown in (a). Cellular uptake of PH-GVs by murine RAW 264.7 macrophage cells were observed under a fluorescence Microscope. Representative images are shown in (b). Scale bars represent 20  $\mu$ m.



(caption on next page)

**Fig. 5.** *In vivo* biodistribution of PH-GVs. (a) *In vivo* NIR fluorescent imaging of tumor-bearing mice was taken at different times after intravenous injection of free ICG, ICG labeled GV, ICG labeled HA-GVs and ICG labeled PH-GVs, respectively. Red circles indicate the tumor's location. (b) Tumor/muscle (T/M) ratio of tumor-bearing mouse model at different times. Data represent the mean  $\pm$  SD from 5 independent experiments. (c) *Ex vivo* fluorescence imaging of vital organs and tumors taken from tumor-bearing nude mice after 4, 12, 24 and 48 h post-injection of ICG-labeled GV, ICG labeled HA-GVs and ICG labeled PH-GVs, respectively. Quantitative analysis for the accumulation in tumor and vital organs of ICG labeled GV, ICG labeled HA-GVs and ICG labeled PH-GVs are shown in (d), (e) and (f). Data represent the mean  $\pm$  SD ( $n = 5$ ). \* $p < 0.05$  vs. control. \*\* $p < 0.01$  vs. control. *In vivo* biodistribution of PH-GVs. (g) Confocal images of tumor slices collected from mice 12 h post-injection of ICG-labeled GV and ICG-labeled PH-GVs. The green and red signals were from the fluorescence of ICG and anti-CD31-stained blood vessels, respectively.

PBS (pH = 7.4). The solution was then stirred in an ice-bath for 2 h. Then 1 mL of GVs (5 nM) dissolved in PBS (pH = 7.4) was added dropwise. The reaction mixture was stirred for another 24 h at 4 °C. The resulting mixture was added into the ultrafiltration tube (2 mL) and centrifuged at 1800 rpm for 5 min to remove free EDC, NHS, and HA. The resultant nanoparticles were stored in PBS buffer 4 °C. PEG was chemically conjugated to the HA-GVs conjugate through amide formation in the presence of EDC and NHS. The HA-GVs conjugate was dissolved in PBS (pH = 7.4), which was mixed with EDC (3.37 mg) and NHS (2 mg) in PBS. After PEG-amine (73.5 mg) was slowly added, the mixture was stirred for 24 h in an ice-bath. The resulting solution was then centrifuged against the excess amount of EDC, NHS and PEG and washed 4 times with PBS.

The prepared GVs were also labeled with a NIR dye, ICG, for cellular experiments and animal imaging tests, as a first step before the addition of HA and PEG [35,36]. Briefly, EDC and NHS were added to ICG solution in PBS (pH = 7.4). After 30 min incubation at room temperature, the solution was added to pure GV solution (molar ratio: ICG/GV = 1000/1). Then the mixture was shaken for 4 h at 4 °C and followed by purification 4 times by centrifugation. The resulting mixture was added into an ultrafiltration tube (50 mL) and centrifuged 1800 rpm for 5 min to remove free ICG. The resultant nanoparticles were stored in PBS buffer.

### 3.3. Characterization of GVs and PH-GVs

The particle size and size distribution of PH-GVs were measured by dynamic light scattering DLS (Varian, Palo Alto, USA). Zeta potential measurements were performed at 25 °C on a Malvern Zeta Size-Nano Z instrument. UV-vis absorbance spectra of GVs and PH-GVs were observed by Multiskan Go microplate reader (Thermo Fisher Scientific, Massachusetts, USA). Fluorescent signals of ICG and ICG labeled PH-GVs were measured using a fluorescence spectrophotometer (Varian, Palo Alto, USA). The morphology of GVs was imaged using transmission electron microscopy (TEM) (JEOL 2100 F, JEOL, Tokyo, Japan) operating at 200 kV. GVs in deionized water (0.5 nM) were deposited on a carbon-coated grid and dried at room temperature overnight. Hydrodynamic size was obtained using the dynamic light scattering (DLS) method.

### 3.4. Acoustic imaging of GVs and PH-GVs *in vitro*

PH-GVs and GVs were put into a dropper (5 mL) before imaging and all the droppers were immersed at the same depth in the deionized water. Ultrasound B-mode and Contrast mode images of GVs were acquired using Vevo 2100 imaging system (FUJIFILM VisualSonics, Toronto, ON, Canada, 21 MHz, B-mode) with a transducer of LZ250 D. The center frequency and output energy level were set to 18 MHz and 4%, respectively.

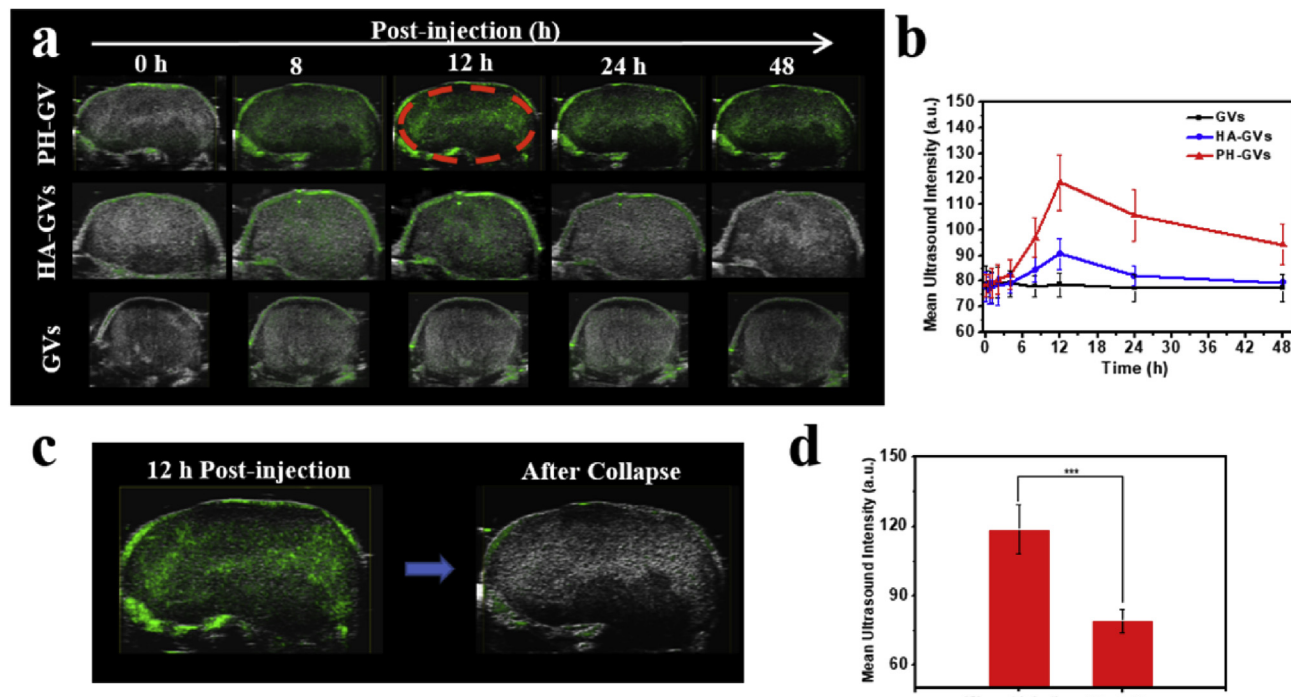


**Fig. 6.** Ultrasound imaging of PH-GVs in tumor sites. *In vivo* ultrasound images of tumor after intravenous injection of GVs, HA-GVs and PH-GVs were captured. Representative images are shown in (a) with quantification of intensity shown in (b). The green color represents the intensity-enhanced region due to the GVs. (c) Vesicle collapse with destructive insonation (650 kPa). Representative images are shown in (c) with quantification of intensity shown in (d). Data represent the mean  $\pm$  SD from 3 independent experiments. \* $p < 0.05$  vs. control. \*\*\* $p < 0.001$  vs. control.

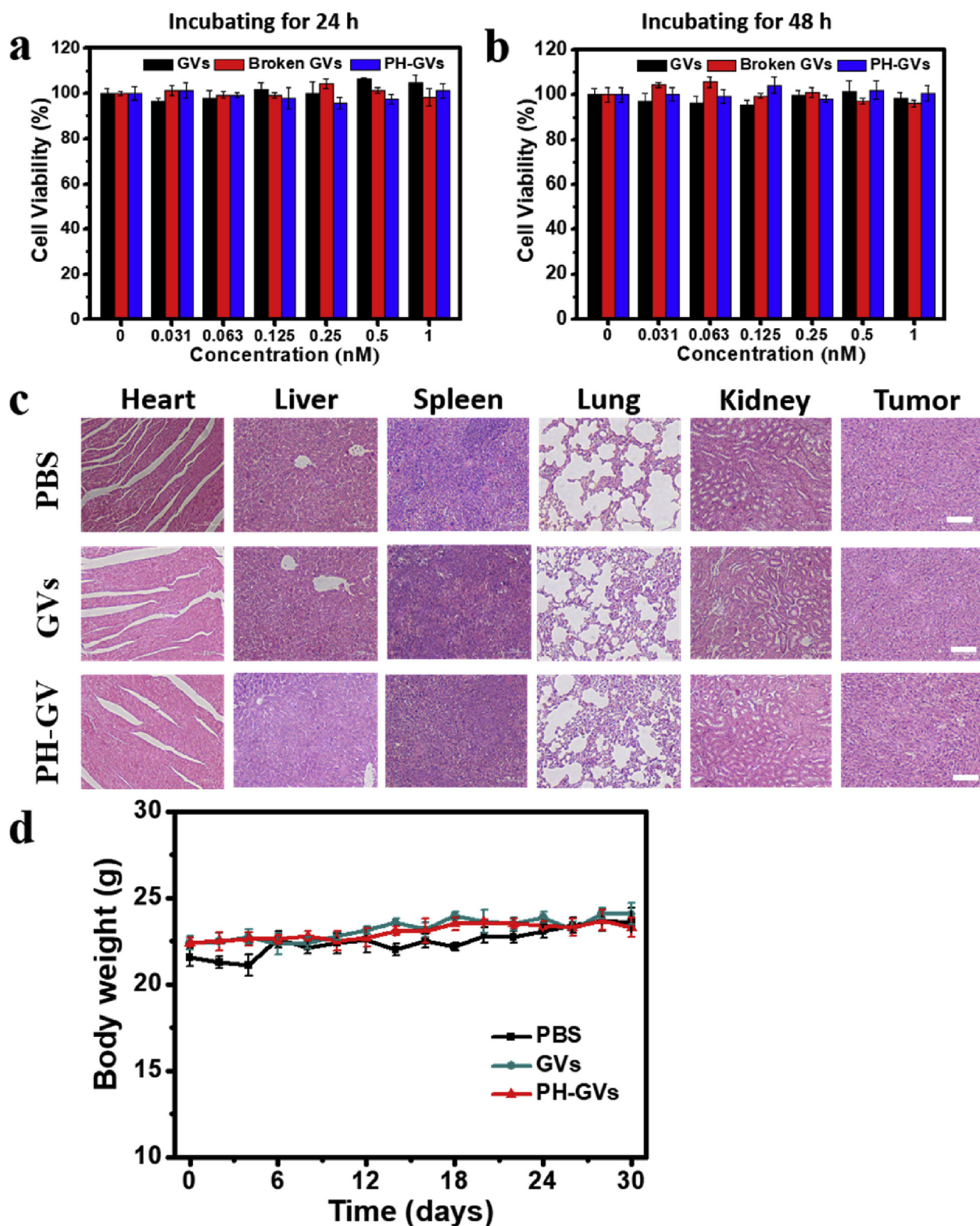


**Fig. 7.** Toxicity of PH-GVs both *in vitro* and *in vivo*. Viability assay of SCC-7 cells after treatment with GVs, collapsed GVs and PH-GVs at the concentration of 0.031–1 nM for 24 h (a) and 48 h (b). (c) Representative H&E sections of the vital organs (heart, liver, spleen, lung, and kidney.) and tumors after GVs/PH-GVs treatment for 30 days. Scale bars, 100  $\mu$ m. (d) Body weights were measured during the 30-day evaluation period in mice under different conditions. Data represent the mean  $\pm$  SD from 4 independent experiments.

### 3.5. Cell internalization detection of GVs and PH-GVs

Human squamous cell carcinoma cell line (SCC7 cells) and murine RAW 264.7 macrophage cells were seeded in an 8-well chamber in

Dulbecco's Modified Eagle Medium (DMEM)/high glucose medium supplemented with 10% FBS and 1% antibiotic solution at 37 °C and 5% CO<sub>2</sub>. The next day, both cells were washed by cold PBS and incubated with different kinds of GVs at 37 °C for 4 h with 5% CO<sub>2</sub> atmosphere.

After incubation, all cells were washed thoroughly with cold PBS. The cells were finally fixed in cold ethanol for 15 min at  $-20^{\circ}\text{C}$  and mounting medium containing DAPI was added and incubated for 10 min in the dark. Cell internalization of ICG labeled PH-GV and ICG labeled GVs were observed by a confocal microscope (Olympus, USA) and the excitation and emission wavelengths were set at 780 nm and 800 nm for ICG, respectively.

### 3.6. Cytotoxicity detection of GVs and PH-GVs

The SCC7 cells were seeded in a 96-well plate at a density of 8000 cells per well and cultured overnight at  $37^{\circ}\text{C}$  in a 5%  $\text{CO}_2$  incubator. The next day, cells were washed with 3 times PBS and incubated with GVs, collapsed GVs and PH-GVs at a series of concentrations for 24 h and 48 h under the same conditions. Cell viability was evaluated by CCK-8 assay kit. The optical density (OD) was measured at 450 nm and recorded by a microplate reader.

### 3.7. Biodistribution of GVs and PH-GVs in nude mice

Animal experiments were conducted under protocols approved by Animal Care and Use Committee (CC/ACUCC) of The Hong Kong Polytechnic University. Subcutaneous sites of athymic nude mice (seven weeks old, female, 20–24 g) were injected with a suspension of  $4 \times 10^6$  SCC7 cells in PBS (80  $\mu\text{l}$ ). When the tumor size (in the right leg region) reached an average size of  $120 \text{ mm}^3$ , mice were randomly allocated into three groups, (a) Free ICG solution was injected into the tail vein of the mice. (b) ICG labeled GVs solution were injected into the tail vein of the mice. (c) ICG labeled PH-GVs solution were injected into the tail vein of the mice. Fluorescence images were acquired at 0, 0.5, 1, 2, 4, 8, 12, 24 and 48 h after injection using IVIS Lumina II (Caliper Life Sciences, USA; Excitation Filter: 780 nm, Emission Filter: 800 nm). At the time of highest accumulation after one-dose injection, tumors and normal organs (heart, liver, spleen, kidney, lung, and muscle) were collected and for acquisition of Fluorescent signal intensity.

### 3.8. In vivo US imaging of SCC7 tumor xenografts in nude mice

US images in the tumor sites were recorded on Vevo 2100 imaging system. When the tumor size (in the right leg region) reached an average size of  $120 \text{ mm}^3$ , mice were randomly allocated into three groups, (a) PBS, (b) GVs and (c) PH-GVs. US imaged were acquired at 0, 0.5, 1, 2, 4, 8, 12, 24 and 48 h following tail injection. At the time of highest accumulation after one-dose injection, a high power of US stimulation is performed, which can induce the collapse of GVs. The signal intensities of echo imaging were measured using Vevo 2100 Workstation Software.

### 3.9. Statistical analysis

Comparisons among groups were analyzed via independent-samples one-factor ANOVA test using SPASS 17.0 software. All statistical data were obtained using a two-tailed student's t-test and homogeneity of variance tests ( $p$  values  $< 0.05$  were considered significant).

### Acknowledgments

The authors would like to thank the facility and technical support from University Research Facility in Life Sciences (ULS) of The Hong Kong Polytechnic University in this work. This work was financially supported through grants from the Research Grant Council (project #15215615 and 15326416), and Natural Science Foundation of China (project # 11674271).

### Appendix A. Supplementary data

Supplementary data to this article can be found online at <https://doi.org/10.1016/j.biomaterials.2020.119803>.

### References

- [1] T. Hussain, Q.T. Nguyen, Molecular imaging for cancer diagnosis and surgery, *Adv. Drug Deliv. Rev.* 66 (2014) 90–100.
- [2] H. Chen, Z. Zhen, T. Todd, P.K. Chu, J. Xie, Nanoparticles for improving cancer diagnosis, *Mater. Sci. Eng. R Rep.* 74 (3) (2013) 35–69.
- [3] Y. Yang, Z. Qiu, X. Hou, L. Sun, Ultrasonic characteristics and cellular properties of Anabaena gas vesicles, *Ultrasound Med. Biol.* 43 (12) (2017) 2862–2870.
- [4] M.S. Muthu, D.T. Leong, L. Mei, S.S. Feng, Nanotheranostics - application and further development of nanomedicine strategies for advanced theranostics, *Theranostics* 4 (6) (2014) 660–677.
- [5] K.K. Shung, Diagnostic ultrasound: past, present, and future, *J. Med. Biol. Eng.* 31 (6) (2011).
- [6] R. Guo, G. Lu, B. Qin, B. Fei, Ultrasound imaging technologies for breast cancer detection and management: a review, *Ultrasound Med. Biol.* 44 (1) (2018) 37–70.
- [7] Q. Huang, Z. Zeng, A review on real-time 3D ultrasound imaging technology, *BioMed Res. Int.* 2017 (2017) 6027029.
- [8] L. Abou-Elkacem, S.V. Bachawal, J.K. Willmann, Ultrasound molecular imaging: moving toward clinical translation, *Eur. J. Radiol.* 84 (9) (2015) 1685–1693.
- [9] N. Deshpande, A. Needles, J.K. Willmann, Molecular ultrasound imaging: current status and future directions, *Clin. Radiol.* 65 (7) (2010) 567–581.
- [10] S. Hernot, A.L. Klibanov, Microbubbles in ultrasound-triggered drug and gene delivery, *Adv. Drug Deliv. Rev.* 60 (10) (2008) 1153–1166.
- [11] D. Cosgrove, C. Harvey, Clinical uses of microbubbles in diagnosis and treatment, *Med. Biol. Eng. Comput.* 47 (8) (2009) 813–826.
- [12] J. Shi, P.W. Kantoff, R. Wooster, O.C. Farokhzad, Cancer nanomedicine: progress, challenges and opportunities, *Nat. Rev. Canc.* 17 (1) (2017) 20–37.
- [13] S. Son, H.S. Min, D.G. You, B.S. Kim, I.C. Kwon, Echogenic nanoparticles for ultrasound technologies: evolution from diagnostic imaging modality to multimodal theranostic agent, *Nano Today* 9 (4) (2014) 525–540.
- [14] T. van Rooij, V. Daeichin, I. Skachkov, N. de Jong, K. Kooiman, Targeted ultrasound contrast agents for ultrasound molecular imaging and therapy, *Int. J. Hyperther.* 31 (2) (2015) 90–106.
- [15] W.B. Cai, H.L. Yang, J. Zhang, J.K. Yin, Y.L. Yang, L.J. Yuan, L. Zhang, Y.Y. Duan, The optimized fabrication of nanobubbles as ultrasound contrast agents for tumor imaging, *Sci. Rep.* 5 (2015) 13725.
- [16] Z. Xing, J. Wang, H. Ke, B. Zhao, X. Yue, Z. Dai, J. Liu, The fabrication of novel nanobubble ultrasound contrast agent for potential tumor imaging, *Nanotechnology* 21 (14) (2010) 145607.
- [17] J. Zhang, Y. Chen, C. Deng, L. Zhang, Z. Sun, J. Wang, Y. Yang, Q. Lv, W. Han, M. Xie, The optimized fabrication of a novel nanobubble for tumor imaging, *Front. Pharmacol.* 10 (2019) 610.
- [18] T. Yin, P. Wang, R. Zheng, B. Zheng, D. Cheng, X. Zhang, X. Shuai, Nanobubbles for enhanced ultrasound imaging of tumors, *Int. J. Nanomed.* 7 (2012) 895–904.
- [19] M.G. Shapiro, P.W. Goodwill, A. Neogy, M. Yin, F.S. Foster, D.V. Schaffer, S.M. Conolly, Biogenic gas nanostructures as ultrasonic molecular reporters, *Nat. Nanotechnol.* 9 (4) (2014) 311–316.
- [20] A. Lakshmanan, A. Farhadi, S.P. Nety, A. Lee-Gosselin, R.W. Bourdeau, D. Maresca, M.G. Shapiro, Molecular engineering of acoustic protein nanostructures, *ACS Nano* 10 (8) (2016) 7314–7322.
- [21] R.W. Bourdeau, A. Lee-Gosselin, A. Lakshmanan, A. Farhadi, S.R. Kumar, S.P. Nety, M.G. Shapiro, Acoustic reporter genes for noninvasive imaging of microorganisms in mammalian hosts, *Nature* 553 (7686) (2018) 86–90.
- [22] D.I. Piraner, A. Farhadi, H.C. Davis, D. Wu, D. Maresca, J.O. Szablowski, M.G. Shapiro, Going deeper: biomolecular tools for acoustic and magnetic imaging and control of cellular function, *Biochemistry* 56 (39) (2017) 5202–5209.
- [23] F. Pfeifer, Distribution, formation and regulation of gas vesicles, *Nat. Rev. Microbiol.* 10 (10) (2012) 705–715.
- [24] J. Le Floch, A. Zlntni, H.A. Bilton, M. Yin, A. Farhadi, N.R. Janzen, M.G. Shapiro, J.F. Valliant, F.S. Foster, In vivo biodistribution of radiolabeled acoustic protein nanostructures, *Mol. Imag. Biol.* 20 (2) (2018) 230–239.
- [25] K.Y. Choi, K.H. Min, H.Y. Yoon, K. Kim, J.H. Park, I.C. Kwon, K. Choi, S.Y. Jeong, PEGylation of hyaluronic acid nanoparticles improves tumor targetability in vivo, *Biomaterials* 32 (7) (2011) 1880–1889.
- [26] K.H. Min, J.H. Kim, S.M. Bae, H. Shin, M.S. Kim, S. Park, H. Lee, R.W. Park, I.S. Kim, K. Kim, I.C. Kwon, S.Y. Jeong, D.S. Lee, Tumoral acidic pH-responsive MPEG-poly(beta-amino ester) polymeric micelles for cancer targeting therapy, *J. Contr. Release* 144 (2) (2010) 259–266.
- [27] A.N. Koo, H.J. Lee, S.E. Kim, J.H. Chang, C. Park, C. Kim, J.H. Park, S.C. Lee, Disulfide-cross-linked PEG-poly(amino acid) copolymer micelles for glutathione-mediated intracellular drug delivery, *Chem. Commun.* (48) (2008) 6570–6572.
- [28] L.J. Cruz, P.J. Tacken, R. Fokkink, C.G. Figdor, The influence of PEG chain length and targeting moiety on antibody-mediated delivery of nanoparticle vaccines to human dendritic cells, *Biomaterials* 32 (28) (2011) 6791–6803.
- [29] V.M. Platt, F.C. Szoka Jr., Anticancer therapeutics: targeting macromolecules and nanocarriers to hyaluronan or CD44, a hyaluronan receptor, *Mol. Pharm.* 5 (4) (2008) 474–486.
- [30] E. Auzenne, S.C. Ghosh, M. Khodadadian, B. Rivera, D. Farquhar, R.E. Price, M. Ravoori, V. Kundra, R.S. Freedman, J. Klostergaard, Hyaluronic acid-paclitaxel:

- antitumor efficacy against CD44(+) human ovarian carcinoma xenografts, *Neoplasia* 9 (6) (2007) 479–486.
- [31] J.D. Byrne, T. Betancourt, L. Brannon-Peppas, Active targeting schemes for nanoparticle systems in cancer therapeutics, *Adv. Drug Deliv. Rev.* 60 (15) (2008) 1615–1626.
- [32] J. Huang, H. Zhang, Y. Yu, Y. Chen, D. Wang, G. Zhang, G. Zhou, J. Liu, Z. Sun, D. Sun, Y. Lu, Y. Zhong, Biodegradable self-assembled nanoparticles of poly (D,L-lactide-co-glycolide)/hyaluronic acid block copolymers for target delivery of docetaxel to breast cancer, *Biomaterials* 35 (1) (2014) 550–566.
- [33] H.S. Qhattal, X. Liu, Characterization of CD44-mediated cancer cell uptake and intracellular distribution of hyaluronan-grafted liposomes, *Mol. Pharm.* 8 (4) (2011) 1233–1246.
- [34] S. Honary, F. Zahir, Effect of zeta potential on the properties of nano-drug delivery systems - a review (Part 2), *Trop. J. Pharmaceut. Res.* 12 (2) (2013).
- [35] K.Y. Choi, K.H. Min, J.H. Na, K. Choi, K. Kim, J.H. Park, I.C. Kwon, S.Y. Jeong, Self-assembled hyaluronic acid nanoparticles as a potential drug carrier for cancer therapy: synthesis, characterization, and *in vivo* biodistribution, *J. Mater. Chem.* 19 (24) (2009) 4102–4107.
- [36] K.Y. Choi, H. Chung, K.H. Min, H.Y. Yoon, K. Kim, J.H. Park, I.C. Kwon, S.Y. Jeong, Self-assembled hyaluronic acid nanoparticles for active tumor targeting, *Biomaterials* 31 (1) (2010) 106–114.